analytical chemistry

pubs.acs.org/ac Article

Imaging Single H_2 Nanobubbles Using Off-Axis Dark-Field Microscopy

Milomir Suvira, Ananya Ahuja, Pascal Lovre, Mantak Singh, Gracious Wyatt Draher, and Bo Zhang*

Cite This: *Anal. Chem.* 2023, 95, 15893−15899 Read Online

ACCESS | Metrics & More | Article Recommendations | Supporting Information

ABSTRACT: A robust and detailed physicochemical description of electrochemically generated surface nanobubbles and their effects on electrochemical systems remains at large. Herein, we report the development and utilization of an off-axis, dark-field microscopy imaging tool for probing the dynamic process of generating single H_2 nanobubbles at the surface of a carbon nanoelectrode. A change in the direction of the incident light is made to significantly reduce the intensity of the background light, which enables us to image both the nanoelectrode and nanobubble on the electrode surface or the metal nanoparticles in the vicinity of the electrode. The correlated electrochemical and optical response provides novel insights regarding bubble nucleation and dissolution on a nanoelectrode previously unattainable solely from its current−voltage response.

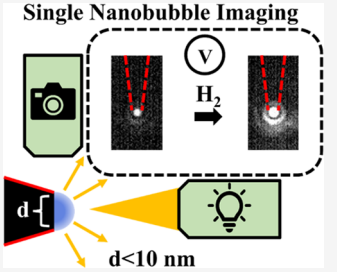

INTRODUCTION

Gaseous products are generated during many important electrochemical reactions. Most notable, electrochemical water splitting produces O_2 and energy-dense H_2 gas molecules at the anode and cathode, respectively.[1] The industrialized chloro-alkali process oxidizes chlorine ions into Cl_2 gas, an important precursor commodity chemical.[2] Additionally, the electrochemical reduction of CO_2 offers a unique platform to remove excess CO_2 from atmospheric or industrial sources while simultaneously producing relevant higher-order carbon products.[3] Nonetheless, CO gas is a critical intermediate or final byproduct of CO_2 reduction.[3] As these gas-evolving electrochemical reactions are typically operated at high current densities to maximize their economic feasibility, the rapid accumulation of gas molecules at the electrode surface inevitability leads to the nucleation, growth, and detachment of gas bubbles.

The presence of nano-, micro-, and macrobubbles on electrode surfaces or in the bulk can have a significant impact on the electrocatalytic surface, mass transfer, and other electrochemically relevant phenomena.[4,5] Additionally, a recent review suggests that bubbles can catalyze nonfaradaic side reactions at the gas−water interface, which may affect the overall electrochemical performance of the desired reactions.[6] Hence, the exploration of bubble properties, including their nucleation, growth, and dissolution/detachment, is critical for the continued improvement of the aforementioned reactions/processes. For example, Wallace and co-workers developed a highly efficient and competitive water electrolysis system by employing a unique cell/electrode design that limits the production of H_2 and O_2 bubbles.[7] We anticipate that fundamental investigations regarding surface nanobubbles will enable further practical technological advancements.

Experimental and theoretical studies estimate that only 35−55 localized gas molecules are required to initiate heterogeneous bubble nucleation on the electrode surface.[8,9] The subsequent formation of a nanometer-sized surface nanobubble can have several fates, including dissolution, coalescence with adjacent bubbles, continued growth, and detachment. Although significant work has been done to explore the physicochemical properties of large bubbles (micro), there remains continued interest in small (nano)bubbles due to their improbable and unique stability.[10] Nonetheless, the size of surface nanobubbles, stochastic generation, optical transparency, and transient nature require specialized analytical tools to probe their characteristics. Specifically, electrochemically generated surface nanobubbles have been studied using a wide range of imaging techniques including atomic force microscopy,[11] interference reflection microscopy,[12] single-molecule total internal reflection fluorescence microscopy,[13] surface plasmon resonance microscopy,[14] scanning transmission X-ray microscopy,[15] and scanning electrochemical cell microscopy (SECCM).[16] Ultimately, the use of these techniques has provided substantial insights into bubble size and nucleation dynamics on different surfaces. However, as these experiments are typically carried out with macroelectrodes where many bubbles are generated and imaged at the same time, the current−voltage response provides little to no information about the individual bubbles and their

Received: May 16, 2023
Accepted: October 4, 2023
Published: October 18, 2023

https://doi.org/10.1021/acs.analchem.3c02132
Anal. Chem. 2023, 95, 15893−15899

associated physicochemical features. The White group has overcome this limitation by generating a single nanobubble on a nanoelectrode where the current−voltage response has been utilized to provide tremendous insight into nucleation rate, growth dynamics, and internal pressure.[17−19] The lack of optical interrogation of single nanobubbles at a nanoelectrode leaves room for exploration and potentially new findings.

Although generating a single nanobubble at a nanoelectrode is advantageous for imaging because of the bubble's unambiguous location at the electrode surface and its high stability with applied voltage, imaging a single bubble at a nanoelectrode has proven to be extremely difficult. One of the biggest challenges is physically integrating an individually addressable nanoelectrode within an imaging platform. For example, nanoelectrodes are typically fabricated using pulled glass capillaries where the end of the fine tip is a nanometer-sized hole that can be used as a template for adding conductive material to yield a nanoelectrode.[20] Although these nanoelectrodes are inherently difficult to make using benchtop methods, there have been numerous reports on different approaches to fabricate them.[21−25] Nonetheless, bulky (insulating glass) and fragile nanoelectrodes require precise control and compatibility with optical systems (i.e., chromatic aberrations from the surrounding glass). Furthermore, to the best of our knowledge, the nanofabrication of optically transparent, individually addressable single nanoelectrodes using advanced lithography techniques has not been reported despite valiant efforts by us and others.

Herein, we report the use of off-axis dark-field microscopy (OADFM) to image a single H_2 nanobubble at a glass-pulled carbon nanoelectrode. We elected to use the conventional glass/quartz-based nanoelectrodes in order to avoid the complexity of nanofabrication. Although traditional dark-field microscopy has been utilized to image many nanobubbles generated at nanoparticle surfaces, the light scattering technique is not compatible with the carbon nanoelectrode due to significant background scattering from the insulating glass material. Thus, we employed a simple modification, perpendicular illumination (off-axis), to enable light scattering only from the electrode surface. Furthermore, by generating a single nanobubble at the electrode surface, we can detect the light scattering from the bubble itself due to its physical presence and change in refractive index at the electrode surface. We utilize the change in light scattering to obtain novel insight regarding nanobubble nucleation and dissolution that has been unattainable solely from the electrochemical response. Although we developed this technique to image single nanobubbles, we anticipate that OADFM will encourage researchers to integrate different electrochemical probes (i.e., nanopores, ultramicroelectrodes, etc.) within the imaging system for label-free investigations in electrochemistry such as nanoparticle translocations through a nanopore and their collisions on an ultramicroelectrode.

EXPERIMENTAL SECTION

Chemicals and Materials. All chemicals and materials were used as received without further modification: Methane (Linde), Argon (Linde), quartz capillaries (Sutter), sulfuric acid (Supelco), potassium ferricyanide (Mallinckrodt), potassium nitrate (Sigma-Aldrich), silver nanoparticles (Nanocomposix), and chlorinated silver wire (Alfa Aesar).

Carbon Nanoelectrode Fabrication. Carbon nanoelectrodes were fabricated using a modified chemical vapor deposition procedure based on several previous reports.[23−25] Glass pipet nanopores were used as templates for carbon deposition. A quartz capillary (1.0 mm O.D. 0.5 mm I.D.) without a filament is pulled using a P2000 laser pipet puller (Sutter) with the following 2-line parameters: HEAT: 710 FIL: 4 VEL: 70 DEL: 132 PUL: 65, HEAT: 760 FIL: 3 VEL: 60 DEL: 127 PUL: 110. Pulling the quartz capillaries creates a roughly circular nanometer-sized hole at the tip glass. The nanopipettes are then inserted into a one inch diameter quartz tube placed within a Mini-Mite tube furnace (Thermo Scientific). Methane and argon gas, at a flow rate of 700 and 100 sccm, respectively, are flowed into the quartz tube antiparallel to the direction of the quartz nanopipette taper. The ends of the quartz tube are sealed with a rubber stopper and tubing to allow gas to flow in and out of the deposition system. A good seal with a rubber stopper/tubing at the inlet and outlet of the quartz tube is critical to ensure consistent gas flow. Next, the tube furnace is ramped to 900 °C from ambient temperature over a period of 45 min to initiate the pyrolysis of methane. The tube furnace is held at 900 °C for an additional 65 min to fully deposit carbon inside the nanopore. The tube furnace is cooled to 800 °C under room temperature conditions before opening. Finally, the furnace continues to cool (opened) until roughly 400 °C before the methane and argon gases are turned off. The newly minted nanoelectrodes are carefully removed from the tube furnace for subsequent visual examination and electrochemical characterization. A schematic, a commentary, and a photo of a carbon nanoelectrode are provided in Figure S1.

Dark-Field Microscopy. In order to image the nanoparticles, nanoelectrodes, and nanobubbles presented in the main text and Supporting Information, we employed both traditional and off-axis darkfield microscopies. All images were recorded at a frame rate of 18.846 frames/second, unless otherwise noted, using a CCD camera (Andor, Clara series). Scattering intensity was extracted using ImageJ, for which a 7 × 7-pixel2 area around the electrode was used to define the region of interest. For conventional darkfield imaging, a high numeral aperture (NA 1.43) darkfield condenser (Nikon) was mounted onto an upright microscope (Olympus, BX51) where an oil drop was used to make contact with a modified plastic cuvette that acts as a sample holder. A carbon nanoelectrode was epoxied on the bottom portion of the cuvette, and then 20 nm-diameter Ag nanoparticles (Nanocomposix) were added into the sample chamber. The nanoelectrode and nanoparticles were illuminated at max intensity by using the built-in light source (100W) from the microscope. A 20× (0.5 NA) objective (Olympus, UPlanFL N) was used for all dark-field measurements (on-axis) (Figure 1).

A schematic and picture of our imaging platform are presented in Figure 2A. In order to achieve off-axis illumination, we constructed a side arm that consisted of several hollow tubes and mounts with a 10× 0.3 NA (Olympus, UPlanFL N) focusing objective at the end. The objective was used without the need of a beam stop in the middle of the objective as required with the dark-field condenser. The purpose of the hollow tubes (no internal optical components) is to extend the length of the objective across the microscope sample stage. The side arm was positioned perpendicular and close to the collecting objective by using a 3-axis micromanipulator (Newport). The purpose of the 3-axis manipulator is to align the focal point of the illumination objective with the focal point of the collecting

https://doi.org/10.1021/acs.analchem.3c02132
Anal. Chem. 2023, 95, 15893−15899

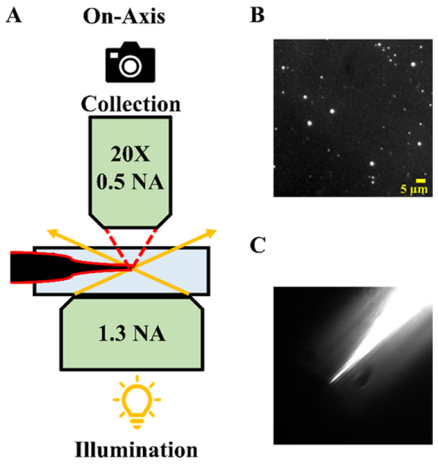

Figure 1. Imaging nanoelectrodes and nanoparticles with traditional "on-axis" Dark-field microscopy. (A) Experimental setup; (B) 20 nm Ag nanoparticles under dark-field illumination; (C) carbon nanoelectrode and 20 nm Ag nanoparticles under dark-field illumination.

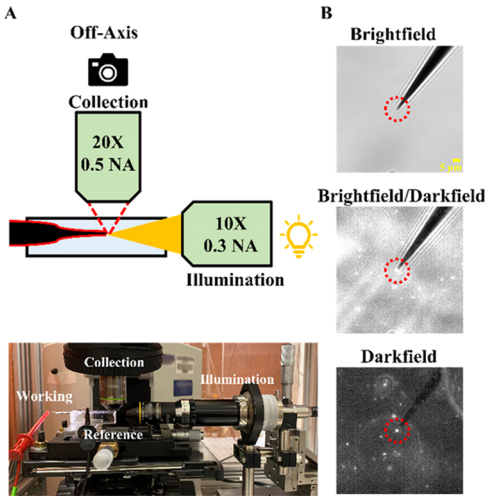

Figure 2. Off-axis dark-field microscopy is used for imaging nanoelectrodes and nanoparticles. (A) Experimental setup, (B) carbon nanoelectrode and 20 nm Ag nanoparticles under brightfield, quasi brightfield/darkfield, and dark-field illumination.

objective where the highest signal-to-noise ratio is achieved. Furthermore, the 3-axis sample stage on the microscope allowed the placement/focusing of the sample (nanoelectrode) within the overlapping illumination and collection region. The fiber optic illumination arm of a 150W halogen lamp (Cole Parmer, 41723 series) was fixed/centered onto a mounting platform and operated at maximum intensity at the base of the hollow tubes. Carbon nanoelectrodes were epoxied on the top side of the fabricated cuvette as this was the ideal location where the two objectives could be manually aligned without bumping into each other or the microscope stage. A 20× (0.5 NA) (Olympus, UPlanFL N) objective was used for the nanoelectrode/bubble imaging.

Electrochemistry. An EG&G Parc 175 waveform generator interfaced to a Dagan Chem-Clamp current amplifier is used to generate cyclic voltammograms for electrode characterization and bubble formation; an in-house Labview program interfaced to a breakout box (National Instruments, BNC 2090-A) is used to record the voltage−current response. Fabricated carbon nanoelectrodes are characterized in an aqueous solution containing 10 mM potassium ferricyanide ($Fe(CN)_6^{3-}$) and 1 M KNO_3 with a Ag/AgCl wire acting as a quasi-reference electrode (QRE). A cyclic waveform from +600 to −600 mV is applied at a scan rate of 50 mV/s to yield the characteristic diffusion-limited response from the one-electron reduction of ferricyanide. Assuming a disk-shaped electrode, the electrode radius, r, is calculated from the diffusion-limited steady-state current, i_{ss}, using the following expression: $i_{ss} = 4nFDC^*r$, where D and C^* are the diffusion coefficient and bulk concentration of $Fe(CN)_6^{3-}$, respectively, F is Faraday's constant, and $n = 1$ is the number of transferred electrons per redox molecule.

A single H_2 nanobubble is generated at the carbon nanoelectrode by applying a cyclic waveform from 0 to −2.5 V vs Ag/AgCl QRE at a scan rate of 100 mV/s in a solution containing 0.5 M H_2SO_4.

RESULTS AND DISCUSSION

Traditional dark-field microscopy employs the use of a high numeral aperture (NA) condenser with a center beam stop in order to illuminate a sample with a highly angled hollow cone of light (Figure 1A). The steep angle of illumination creates a dark image background because the incident light does not enter the collecting objective that ultimately focuses the light onto the detector. The presence of an object within the focus of the illuminating light, say a nanoparticle, can redirect the light (scattering) in many directions due to change in refractive index (liquid vs solid vs gas),[26] interactions with an objects' surface plasmons,[27] and elastic scattering;[28] some of this light can be easily captured by the collecting objective. As the scattering light only comes from the object of interest against a dark background, the high signal-to-noise ratio enables label-free imaging of objects well below the diffraction limit of light; Figure 1B shows 20 nm diameter silver nanoparticles under dark-field illumination (on-axis). Thus, dark-field microscopy is a useful analytical tool to image surface nanobubbles and other phase change phenomena at the electrode surface as demonstrated by several others.[29−34]

Imaging a single nanobubble at a nanoelectrode, however, is difficult using traditional dark-field microscopy due to the significant light scattering from the insulating glass material needed for nanoelectrode fabrication. For example, the nanoelectrode saturates the detector during dark-field illumination such that the detection of the silver nanoparticles is no longer possible (Figure 1C). As it is necessary to image the sub-10 nm electrode surface at the end of the glass tip during bubble nucleation, we needed to change the nature of the dark-field illumination. We were able to overcome the light scattering from the glass by producing "dark-field light" through off-axis illumination with respect to the collection objective (Figure 2A). By using a low-NA objective oriented perpendicular to the collection objective to direct the incident light, the majority of the incident white light never reaches the camera, while objects within the light path, the nanoelectrode and nanoparticles, are easily visible (Figure 2B and Video S1). A similar approach was employed via light-sheet microscopy to visualize plasmonic nanoparticles during movement through a capillary.[35] Yet, it is important to note that our illumination technique does not require light sheet formation or a center beam stop at the illumination objective for a hollow cone of incident light. Additionally, off-axis illumination, without light focusing, was utilized by the Kanoufi group to study submicron nanoparticle nucleation and growth dynamics at nano-

https://doi.org/10.1021/acs.analchem.3c02132
Anal. Chem. 2023, 95, 15893−15899

electrodes.[33,34] One of the advantages in using off-axis illumination is the ability to physically integrate an electrochemical probe within the imaging platform without the need for complex positioning components (i.e., piezo manipulators) to bring the probe near the coverslip as required by traditional darkfield (due to the high angle focusing). To date, we have explored the use of the OADFM to image nanoparticle translocations at conical glass nanopores and nanoparticle collisions at carbon fiber ultramicroelectrodes. A major requirement for the use of this technique is to avoid the bulky insulating material surrounding the electrode or pore that increases the background signal. A more technical and detailed description of our imaging platform is provided in the Experimental Section.

Carbon nanoelectrodes were fabricated by pyrolyzing methane gas within a conical glass nanopore, which ultimately results in confined carbon deposition to produce a nanoelectrode at the tip. Each fabricated nanoelectrode is electrochemically characterized to determine the electrode quality, size, and usefulness for bubble nucleation. A detailed and comprehensive procedure is provided in the experimental section and Supporting Information (Figure S1). In order to generate a single H_2 nanobubble at the carbon electrode, we scanned the electrode from 0 to −2.5 V and back to 0 V in 0.5 M H_2SO_4 at a scan rate of 100 mV/s (Figure 3). The standard

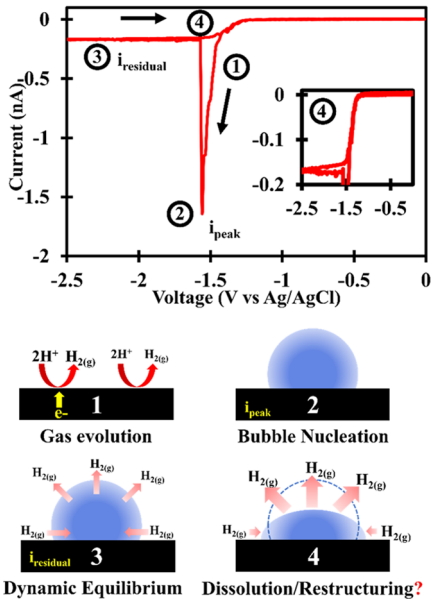

Figure 3. Generating a single H_2 nanobubble on the surface of a carbon nanoelectrode. Top, characteristic voltammetric response of a carbon electrode in 0.5 M H_2SO_4 showing the increase in the cathodic HER current at the beginning of the trace, the sudden current drop due to bubble formation, and the sigmoidal $i-V$ curve on the reverse scan. Bottom schematics showing HER, bubble formation, reaching the equilibrium, and bubble dissolution at the four different stages marked in the CV response.

electrode potential for the hydrogen evolution reaction (HER), $2H^+ + 2e^- \leftrightarrow H_{2(g)}$, versus the Ag/AgCl quasi-reference electrode, is −0.22 V. As carbon is a poor electrode material for HER, the increase in cathodic current after ∼−1.2 V vs Ag/AgCl indicates H_2 gas production at the electrode surface (Figure 3). The rapid accumulation of H_2 gas molecules at continued reducing potentials creates a supersaturated environment poised for nanobubble nucleation. The characteristic drop in the cathodic current at the peak current, i_{peak}, indicates the successful heterogeneous nucleation of a single nanobubble (Figure 3).[36] The bubble covers a majority of the electrode, which limits the available electrocatalytic surface for continued H_2 production. However, there remains a nonzero residual current, $i_{residual}$, that indicates the continued presence of the bubble at the electrode surface (Figure 3).[36] More importantly, the residual current is used to sustain the nanobubble by continuously producing H_2 gas for influx into the bubble in order to compensate for gas outflux from the bubble. Indeed, the dynamic equilibrium between gas influx and outflux has been used to explain the unique nanobubble stability.[37]

On the reverse scan (−2.5−0 V), the residual current is maintained until it begins to slowly decrease while scanning more anodic (inset Figure 3). Although the decrease in current in the reverse scan has not been explicitly assigned to any physical change at the electrode/bubble surface in previous reports, we speculated that this region indicates bubble restructuring/dissolution (Figure 3). Scanning more anodic in region 4 can lead to several electrochemical and bubble processes that complicate the interpretation of the physical landscape at the electrode surface. First, scanning more positive leads to a decrease in the rate of HER, which, in turn, can partially contribute to a decrease in the cathodic current. Second, as the rate of gas outflux begins to outcompete gas influx in region 4 due to the decrease in the rate of HER, we anticipate that the bubble begins to dissolve such that its physical shape and adhesion to the electrode surface changes. However, the nature of this dissolution and restructuring is unclear from changes in current alone; for example, it is not clear where the bubble fully disappears from the electrode surface. Thus, we saw a unique opportunity to utilize our OADFM to image the nanobubbles in order to better understand the physical phenomenon at play.

Figure 4A shows the experimental setup for imaging a single H_2 nanobubble under electrochemical conditions using off-axis dark-field microscopy. In short, a carbon nanoelectrode is used to electrochemically generate a single H_2 nanobubble while the microscope simultaneously monitors the scattering intensity at the electrode surface. Figure 4B shows the correlated electrochemical and optical responses of a carbon nanoelectrode with an apparent radius of 3.5 nm during the formation of a single nanobubble (forward scan). The adjacent images are extracted from Video S2. As the cathodic current increases with increasing driving force for the HER, we observe no light scattering changes at the electrode surface (Figure 4B). However, at the peak current, indicative of bubble nucleation, we observe a significant change in the light scattering intensity. The nucleation of a surface nanobubble would inevitably cause changes/increase in scattered light due to an increase in available surface for light scattering and due to a change in refractive index near the electrode surface (i.e., liquid to gas). We provide several examples in the Supporting Information (Figure S2). It is worth mentioning that the dimensions of the nanobubble are unknown despite the known "footprint" or "contact point" based on the calculated electrode size. Based on the change of the scattered light signal, it is likely that the size of the formed nanobubble is greater than the electrode size. Nevertheless, we are hesitant to provide any size information on the nanobubble, as it would be quite remarkable to image the formation of sub-10 nm bubbles (assuming hemispherical shape) using such a simple optical

https://doi.org/10.1021/acs.analchem.3c02132
Anal. Chem. 2023, 95, 15893−15899

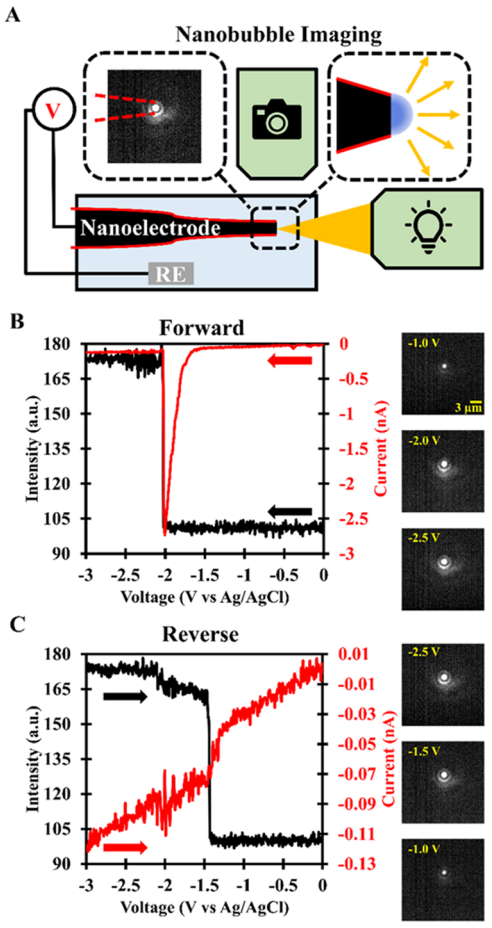

Figure 4. Imaging a single H_2 nanobubble by using OADFM. (A) Experimental setup, (B) correlated electrochemical (red)/optical (black) response and corresponding images in the forward, and (C) reverse voltammetric scan during the formation of a single H_2 nanobubble.

platform. A more thorough investigation of the nanobubble dimensions is needed to verify the absolute size limit of our imaging system.

Simulation and theory have suggested that continued driving force at the electrode surface during bubble generation may lead to an increase in the bubbles' z-profile while retaining the same footprint (radius) as evidenced by a constant residual current.[9] Thus, a change in the bubble size would likely result in more light scattering. However, the optical response shows a constant level of light scattering, which suggests that the bubble's shape/size is static throughout the forward voltammetric scan (Figure 4B). Nonetheless, it is also possible that the changes in the bubble size are too small to detect using a dark field. Additionally, we have verified the quick dissolution (<10 ms) of the nanobubble upon removal of the H_2 gas influx by stepping to open circuit potential to stop HER (data not shown). This result undoubtedly validates the dynamic equilibrium hypothesis used to explain bubble stability.

The electrochemical and optical responses in the reverse scan are presented in Figure 4C. The optical and electrochemical response remains mostly unchanged in the reverse scan. The slight decrease in current even in regions where HER should not occur indicates a "leaky" electrode where ionic current is allowed to pass. However, upon scanning more anodic of −2.0 V, we see a correlated change in both current and scattering intensity. We provide more examples of this phenomenon in the Supporting Information (Figure S2). Thus, we are once again faced with the problem of interpreting the physical nature of the bubble response in region 4 as previously described. Before we explore our results, we would like to clarify that our use of the word "dissolution" refers to the bubble state where the gas outflux begins to outcompete gas influx as opposed to referring to gas outflux as a whole; indeed, Zhang and co-workers have demonstrated continuous gas outflux from surface nanobubbles.[38] Rapid bubble dissolution (faster than the 18.846 Hz frame rate) or sudden detachment would result in a step (on−off) light scattering response, as demonstrated in the forward scan upon bubble nucleation (Figure 4B). However, we observe an extended decay in the scattering intensity followed by a sharp decrease in the baseline (Figures 4C and S2). As light scattering is related to the size of an object, we suggest that the decay in the bubble scattering intensity results from the bubble decreasing in size while remaining attached to the electrode. A detailed understanding of the bubble size and shape is needed to provide more precise insight into the effects of changing bubble features on changes in scattering intensity. As this proposed change in size is correlated with a gradual decrease in cathodic current, gas outflux from the bubble must dominate gas influx into the bubble. It is worth highlighting that the point where the optical and electrochemical curves cross indicates that the bubble is no longer present on the electrode surface; this insight is not accessible from the electrochemical response alone (Figures 4C and S2). The optical response is highly reproducible during each bubble nucleation step for a given electrode despite some greater variations in the current (Figure 5). As each cyclic voltammogram is an independent

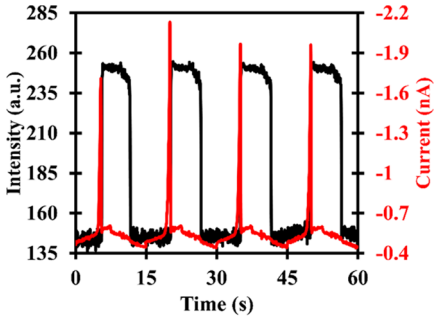

Figure 5. Optical (black) and electrochemical (red) responses during four consecutive CV scans from 0 to −3 V at a scan rate of 400 mV/s.

nanobubble nucleation and growth event, it is likely that the size and shape of the resulting nanobubble are more constant, which determines the magnitude of the scattered optical signal. On the other hand, the peak current may be more affected by the fast nucleation kinetics and the somewhat limited instrument bandwidth. Interestingly, the nature of the scattering response, particularly in the dissolution region, does not change much with different scan rates (Figure S3).

Nonetheless, the nature of the bubble's dissolution remains elusive. For example, does the bubble retain its footprint (radius) while it dissolves in the z direction? In order to better understand the bubble's fate in region 4, we resort to the Young−Laplace equation where $\Delta P = P_{H2(g)} - P_{ext}$ represents the Laplace pressure, where $P_{H2(g)}$ is the internal pressure and

https://doi.org/10.1021/acs.analchem.3c02132
Anal. Chem. 2023, 95, 15893−15899

P_{ext} is the applied pressure (atmospheric), γ is the surface tension, and R is the bubble radius of curvature (eq 1).

$$\Delta P = P_{H_2(g)} - P_{ext} = \frac{2\gamma}{R} \quad (1)$$

The sustained outflux of gas would inevitably lead to a decrease in the bubble's internal pressure. As the Laplace pressure decreases, assuming surface tension remains constant, the bubble has access to different bubble shapes (i.e., radius of curvature) that are determined by the contact angle and radius. Hence, the decrease in cathodic current/scattering in region 4 may result due to a decrease in bubble contact angle that permits an increase in bubble radius/footprint, which in turn blocks more of the electrode surface responsible for HER (dynamic r). The dynamic and ever-changing nature of the gas−water interface has been used as a possible mechanism for explaining nanobubble stability.[34] Additionally, simulation has predicted an increasing contact angle (expanding footprint) during the dissolution of a surface nanobubble.[39] Alternatively, the bubble may remain pinned to the electrode surface (static footprint) where a decrease in the cathodic current would result due to a decrease in driving force for HER while the decrease in light scattering would indicate dissolution of a pinned bubble (constant r). Additionally, we anticipate that a decrease in the bubble's footprint (receding r) during dissolution would lead to an increase in the cathodic current as more electrode area would be exposed; we have not observed any evidence of this in the present report. A simple schematic outlining our hypothesis is provided in Figure S4. Still, the on−off step in the optical scan after the decay region limits our understanding of the entire bubble dissolving process, as the scattering response may indicate bubble detachment (on−off) as opposed to true dissolution. The bubble dissolution process at this point may be too fast to detect optically. More work is needed to determine whether the bubble fully dissolves or detaches and becomes a bulk nanobubble. Although the stability of bulk nanobubbles continues to be an intense topic of debate, we are more inclined to believe in the complete dissolution of the nanobubble once the driving force for gas influx is removed.[40]

CONCLUSIONS

We have introduced off-axis dark-field microscopy as a simple yet powerful tool to image the formation of a single nanobubble at a carbon nanoelectrode. A simple change in the direction of the incident light allows us to significantly lower the background light scattering in imaging nanoelectrochemical processes, which are somewhat prohibitive when using conventional dark-field microscopies. The correlated optical and electrochemical responses reveal that the nanobubbles nucleate on the electrode surface, as evidenced by the stepwise increase in light scattering and sudden drop in current. Additionally, we provide some insight into the nature of nanobubble dissolution during the reverse voltammetric scan. We observe a gradual decrease in light scattering intensity followed by a stepwise decrease to baseline as the cathodic current begins to decrease, which suggests bubble restructuring during the gas outflux phase.

Despite its power in observing a nanobubble's nucleation process, the temporal resolution of the current system is rather limited. One way to improve the temporal resolution (i.e., μs) for future investigations is to use a high-power illumination source such as a laser over the halogen lamp used in this study.

ASSOCIATED CONTENT

Supporting Information

The Supporting Information is available free of charge at https://pubs.acs.org/doi/10.1021/acs.analchem.3c02132.

Carbon nanoelectrode fabrication/characterization, optical/electrochemical response in the forward/reverse scan, optical response varying scan rate, and tentative hypothesis for bubble dissolution (PDF)

Video imaging nanoparticle/nanoelectrode (Video S1) (AVI)

Video imaging a single nanobubble (Video S2) (AVI)

AUTHOR INFORMATION

Corresponding Author

Bo Zhang − *Department of Chemistry, University of Washington, Seattle, Washington 98195-1700, United States;* orcid.org/0000-0002-1737-1241; Phone: 1-206-543 1767; Email: zhangb@uw.edu; Fax: 1-206-685-8665

Authors

Milomir Suvira − *Department of Chemistry, University of Washington, Seattle, Washington 98195-1700, United States;* orcid.org/0000-0003-2086-1388

Ananya Ahuja − *Department of Chemistry, University of Washington, Seattle, Washington 98195-1700, United States*

Pascal Lovre − *Department of Chemistry, University of Washington, Seattle, Washington 98195-1700, United States;* orcid.org/0009-0000-3534-2826

Mantak Singh − *Department of Chemistry, University of Washington, Seattle, Washington 98195-1700, United States*

Gracious Wyatt Draher − *Department of Chemistry, University of Washington, Seattle, Washington 98195-1700, United States*

Complete contact information is available at: https://pubs.acs.org/10.1021/acs.analchem.3c02132

Notes

The authors declare no competing financial interest.

ACKNOWLEDGMENTS

The authors gratefully acknowledge financial support from the National Science Foundation (CHE-2203609).

REFERENCES

(1) Li, X.; Zhao, L.; Yu, J.; Liu, X.; Zhang, X.; Liu, H.; Zhou, W. *Nano-Micro Lett.* **2020**, *12*, 1−29.

(2) Crook, J.; Mousavi, A. *Environ. Forensics* **2016**, *17*, 211−217.

(3) Jin, S.; Hao, Z.; Zhang, K.; Yan, Z.; Chen, J. *Angew. Chem., Int. Ed.* **2021**, *133*, 20795−20816.

(4) Zhao, X.; Ren, H.; Luo, L. *Langmuir* **2019**, *35*, 5392−5408.

(5) Angulo, A.; van der Linde, P.; Gardeniers, H.; Modestino, M.; Rivas, D. F. *Joule* **2020**, *4*, 555−579.

(6) Ciampi, S.; Iyer, K. S. *Curr. Opin. Electrochem.* **2022**, *34*, 100992.

(7) Hodges, A.; Hoang, A. L.; Tsekouras, G.; Wagner, K.; Lee, C. Y.; Swiegers, G. F.; Wallace, G. G. *Nat. Commun.* **2022**, *13*, No. 1304.

(8) Edwards, M. A.; White, H. S.; Ren, H. *ACS Nano* **2019**, *13*, 6330−6340.

(9) Perez Sirkin, Y. A.; Gadea, E. D.; Scherlis, D. A.; Molinero, V. *J. Am. Chem. Soc.* **2019**, *141*, 10801−10811.

(10) Tan, B. H.; An, H.; Ohl, C. D. *Curr. Opin. Colloid Interface Sci.* **2021**, *53*, 101428.

(11) Mita, M.; Matsushima, H.; Ueda, M.; Ito, H. *J. Colloid Interface Sci.* **2022**, *614*, 389−395.

(12) Lemineur, J. F.; Ciocci, P.; Noël, J. M.; Ge, H.; Combellas, C.; Kanoufi, F. *ACS Nano* **2021**, *15*, 2643−2653.
(13) Hao, R.; Fan, Y.; Howard, M. D.; Vaughan, J. C.; Zhang, B. *Proc. Natl. Acad. Sci. U.S.A.* **2018**, *115*, 5878−5883.
(14) Wang, Y.; Yuan, T.; Su, H.; Zhou, K.; Yin, L.; Wang, W. *ACS Sens.* **2021**, *6*, 380−386.
(15) Zhou, L.; Wang, X.; Shin, H. J.; Wang, J.; Tai, R.; Zhang, X.; Fang, H.; Xiao, W.; Wang, L.; Wang, C.; Gao, X.; Hu, J.; Zhang, L. *J. Am. Chem. Soc.* **2020**, *142*, 5583−5593.
(16) Liu, Y.; Jin, C.; Liu, Y.; Ruiz, K. H.; Ren, H.; Fan, Y.; White, H.; Chen, Q. *ACS Sens.* **2021**, *6*, 355−363.
(17) Soto, Á. M.; German, S. R.; Ren, H.; Van Der Meer, D.; Lohse, D.; Edwards, M. A.; White, H. S. *Langmuir* **2018**, *34*, 7309−7318.
(18) Liu, Y.; Edwards, M. A.; German, S. R.; Chen, Q.; White, H. S. *Langmuir* **2017**, *33*, 1845−1853.
(19) German, S. R.; Edwards, M. A.; Chen, Q.; White, H. S. *Nano Lett.* **2016**, *16*, 6691−6694.
(20) Hao, R.; Zhang, B. *Anal. Chem.* **2016**, *88*, 614−620.
(21) Li, Y.; Bergman, D.; Zhang, B. *Anal. Chem.* **2009**, *81*, 5496−5502.
(22) Wilde, P.; Quast, T.; Aiyappa, H. B.; Chen, Y. T.; Botz, A.; Tarnev, T.; Marquitan, M.; Feldhege, S.; Linder, A.; Andronescu, C.; Schuhmann, W. *ChemElectroChem* **2018**, *5*, 3083−3088.
(23) Schrlau, M. G.; Falls, E. M.; Ziober, B. L.; Bau, H. H. *Nanotechnology* **2008**, *19*, 015101.
(24) Singhal, R.; Bhattacharyya, S.; Orynbayeva, Z.; Vitol, E.; Friedman, G.; Gogotsi, Y. *Nanotechnology* **2010**, *21*, 015304.
(25) Rees, H. R.; Anderson, S. E.; Privman, E.; Bau, H. H.; Venton, B. J. *Anal. Chem.* **2015**, *87*, 3849−3855.
(26) Novo, C.; Funston, A. M.; Pastoriza-Santos, I.; Liz-Marzan, L. M.; Mulvaney, P. *J. Phys. Chem. C* **2008**, *112*, 3−7.
(27) Liu, M.; Chao, J.; Deng, S.; Wang, K.; Li, K.; Fan, C. *Colloids Surf., B* **2014**, *124*, 111−117.
(28) Shi, R.; Chen, X.; Huo, J.; Guo, S.; Smith, Z. J.; Chu, K. *J. Biophotonics* **2022**, *15*, No. e202100185.
(29) Xu, S.; Yu, X.; Chen, Z.; Zeng, Y.; Guo, L.; Li, L.; Luo, F.; Wang, J.; Qiu, B.; Lin, Z. *Anal. Chem.* **2020**, *92*, 9016−9023.
(30) Ma, Y.; Highsmith, A. L.; Hill, C. M.; Pan, S. *J. Phys. Chem. C* **2018**, *122*, 18603−18614.
(31) Zhang, T.; Li, S.; Du, Y.; He, T.; Shen, Y.; Bai, C.; Huang, Y.; Zhou, X. *J. Phys. Chem. Lett.* **2018**, *9*, 5630−5635.
(32) Wusimanjiang, Y.; Ma, Y.; Lee, M.; Pan, S. *Electrochim. Acta* **2018**, *269*, 291−298.
(33) Brasiliense, V.; Clausmeyer, J.; Dauphin, A. L.; Noel, J. M.; Berto, P.; Tessier, G.; Schuhmann, W.; Kanoufi, F. *Angew. Chem., Int. Ed.* **2017**, *56*, 10598−10601.
(34) Brasiliense, V.; Clausmeyer, J.; Berto, P.; Tessier, G.; Combellas, C.; Schuhmann, W.; Kanoufi, F. *Anal. Chem.* **2018**, *90*, 7341−7348.
(35) Cao, X.; Feng, J.; Pan, Q.; Xiong, B.; He, Y.; Yeung, E. S. *Anal. Chem.* **2017**, *89*, 2692−2697.
(36) Chen, Q.; Luo, L.; Faraji, H.; Feldberg, S. W.; White, H. S. *J. Phys. Chem. Lett.* **2014**, *5*, 3539−3544.
(37) Ma, Y.; Guo, Z.; Chen, Q.; Zhang, X. *Langmuir* **2021**, *37*, 2771−2779.
(38) German, S. R.; Wu, X.; An, H.; Craig, V. S.; Mega, T. L.; Zhang, X. *ACS Nano* **2014**, *8*, 6193−6201.
(39) Zargarzadeh, L.; Elliott, J. A. *Langmuir* **2016**, *32*, 11309−11320.
(40) Zhou, L.; Wang, S.; Zhang, L.; Hu, J. *Curr. Opin. Colloid Interface Sci.* **2021**, *53*, 101439.

https://doi.org/10.1021/acs.analchem.3c02132
Anal. Chem. 2023, 95, 15893−15899